# Gap solitons in a one-dimensional driven-dissipative topological lattice

Nicolas Pernet, Philippe St-Jean, Dmitry Solnyshkov, Guillaume Malpuech, Nicola Carlon Zambon, Quentin Fontaine, Bastian Real, Omar Jamadi, Aristide Lemaitre, Martina Morassi, et al.

# Gap solitons in a 1D driven-dissipative topological lattice

N. Pernet,[1,*] P. St-Jean,[1,*] D.D. Solnyshkov,[2,3] G. Malpuech,[2] N. Carlon Zambon,[1]
Q. Fontaine,[1] B. Real,[4] O. Jamadi,[4] A. Lemaître,[1] M. Morassi,[1] L. Le Gratiet,[1]
T. Baptiste,[1] A. Harouri,[1] I. Sagnes,[1] A. Amo,[4] S. Ravets,[1] and J. Bloch[1]

[1] *Université Paris-Saclay, CNRS, Centre de Nanosciences et de Nanotechnologies (C2N), 91120, Palaiseau, France*

[2] *Institut Pascal, PHOTON-N2, Université Clermont Auvergne, CNRS, SIGMA Clermont, F-63000 Clermont-Ferrand, France.*

[3] *Institut Universitaire de France (IUF), 75231 Paris, France*

[4] *Université de Lille, CNRS, Laboratoire de Physique des Lasers Atomes et Molécules (PhLAM), 59000 Lille, France*

(Dated: November 29, 2021)

**Nonlinear topological photonics is an emerging field aiming at extending the fascinating properties of topological states to the realm where interactions between the system constituents cannot be neglected. Interactions can trigger topological phase transitions, induce symmetry protection and robustness properties for the many-body system. Here, we report on the nonlinear response of a polariton lattice implementing a driven-dissipative version of the Su-Schrieffer-Heeger model. We first demonstrate the formation of topological solitons bifurcating from a linear topological edge state. We then focus on the formation of dissipative gap solitons in the bulk of the lattice and show that they exhibit robust nonlinear properties against defects, thanks to the underlying sublattice symmetry. Leveraging on the driven-dissipative nature of the system, we discover a new class of bulk gap solitons with high sublattice polarization. We show that these solitons provide an all-optical way to create a non-trivial interface for Bogoliubov excitations. Our results show that coherent driving can be exploited to stabilize novel many-body phases and establish dissipatively stabilized solitons as a powerful resource for nonlinear topological photonics.**

The topology of band structures in periodic systems is related to the existence of a non-zero Berry phase, and gives rise to fascinating phenomena like anomalous velocity, chiral edge states that are robust to disorder or topological pumps [1, 2]. First discovered in solid-state systems, topological physics can also be emulated in artificial lattices, including atomic [3], photonic [4, 5], mechanical [6], optomechanical [7], and polaritonic [8, 9] systems. These platforms have allowed engineering topological phases hardly achievable in condensed matter, involving synthetic dimensions [10], disorder effects [11, 12], quasi-crystalline structures [13] or higher-order multipoles [14, 15]. The physics becomes even richer when inter-particle interactions are considered [16]. In the weakly interacting regime, nonlinearities can induce topological phase transitions [17–19], wave-mixing among topological modes [20, 21], enable the formation of solitons in a topologically non trivial gap [22–26] or the realization of Thouless pumping with solitons [27–29]. In the strongly interacting regime, novel symmetry protected phases may appear [30], and fractional quantum Hall physics can be emulated with the possible stabilization of multi-particle Laughlin states [31].

Recently, photonic platforms have allowed pushing this exploration beyond the realm of conservative Hamiltonians, mainly through the engineering of gain and loss. Non-Hermitian topological systems [32] have led, for example, to the development of topological lasing on 0D [33–36] or 1D [37, 38] edge states, and PT-symmetric phases [39, 40]. Most of these works on non-Hermitian topology have focused on probing, stabilizing or amplifying the linear response of the system. These recent advances now offer the possibility to experimentally explore topological photonics in a regime where non-Hermiticity and nonlinearity are combined [40–43]. Driven-dissipative photonic platforms are particularly suitable to probe this physics because in addition to the non-Hermiticity of the Hamiltonian, the external drive can be used to stabilize novel nonlinear solutions going beyond what is possible in systems subject solely to gain and loss, and to modify the underlying topology [44].

In this article, we investigate the physics of gap solitons in a 1D driven-dissipative topological lattice. We emulate a nonlinear version of the well-known Su-Schrieffer-Heeger (SSH) model: a 1D bipartite topological lattice with staggered hopping energies forming a chain of coupled dimers. [45]. Cavity polaritons are well suited for exploring this nonlinear topological physics [8, 9, 34, 46–48]. Indeed, their excitonic fraction provides repulsive interactions, resulting in a Kerr-type nonlinearity, while their photonic component makes the system intrinsically non-Hermitian via loss and possibly gain. Moreover the system can be resonantly

driven by an external source and reach a steady-state determined by the balance between drive, dissipation and nonlinearity [49].

We demonstrate the formation of dissipative solitons that bifurcate either from a topological interface state or from dimers in the lattice bulk. When excited within the topological gap, the solitons present tails that are highly sublattice polarized. This endows them with robustness properties that we probe using an optically controlled non-Hermitian defect (i.e. a local perturbation to the real and imaginary parts of the potential landscape). We demonstrate that these solitons are robust to defects located on one sublattice, a property inherited from the chiral symmetry of the underlying model. The crucial asset brought by the driven-dissipative character of the system appears when engineering the phase of the driving field. By imposing a phase frustration between the phase pattern of the driving field and that of the Bloch eigenstates, we demonstrate the generation of novel gap solitons that have no counterpart in conservative systems and show high sublattice polarization in the core. Crucially, we show how the modification of the potential landscape induced by these asymmetric solitons can effectively split the chain and form a non-trivial interface. This latter aspect is evidenced through the emergence of a topological edge state in the calculated Bogoliubov excitation spectrum.

## THE NONLINEAR DRIVEN-DISSIPATIVE SSH MODEL

The physics of the polariton nonlinear SSH model can be captured by a discretized Gross-Pitaevskii equation in presence of drive and dissipation:

$$i\hbar\frac{d}{dt}\begin{bmatrix}a_n\\b_n\end{bmatrix} = \left(E_0 - i\frac{\gamma}{2}\right)\begin{bmatrix}a_n\\b_n\end{bmatrix} + g\begin{bmatrix}|a_n|^2 a_n\\|b_n|^2 b_n\end{bmatrix} - J\begin{bmatrix}b_n\\a_n\end{bmatrix} - J'\begin{bmatrix}b_{n-1}\\a_{n+1}\end{bmatrix} + i\begin{bmatrix}F_{a,n}\\F_{b,n}\end{bmatrix}e^{i\omega t} \quad (1)$$

where $\boldsymbol{\psi}_n = [a_n; b_n]^T$ is a spinor describing the wavefunction of the A and B sites in the $n^{th}$ unit cell; $E_0$ is the on-site energy,$\gamma$ the polariton linewidth, $g$ the interaction energy, $J$ ($J'$) is the intracell (intercell) coupling energy, and $\omega/(2\pi)$ the driving field frequency which sets the frequency of the polariton field. The driving field $\boldsymbol{F}_n = [F_{a,n}; F_{b,n}]^T$ can be engineered with a specific amplitude and phase on each site, $F_{\alpha,n} = |F_{\alpha,n}|e^{i\varphi_{\alpha,n}}$.

The topological nature of the SSH model is related to chiral (or sublattice) symmetry, which imposes identical on-site energies and restricts the coupling terms to sites belonging

to distinct sublattices, e.g. no next-nearest neighbour coupling. Zero-energy states which emerge in lattices ending with weak links are protected by this symmetry. They are localised on a single sublattice, thus presenting well defined sublattice pseudo-spin:

$$\tilde{S} = \frac{\sum_n |a_n|^2 - |b_n|^2}{\sum_n |a_n|^2 + |b_n|^2} = \pm 1, \tag{2}$$

The sign of the spin reflects the sublattice localization, either on $A$ (+1) or $B$ (-1). The existence of topological edge states can also be related to the value of the winding number $\mathcal{W}$ computed over the first Brillouin zone [50] that can take the values 0 (strong link termination) or 1 (weak link termination). Hereafter, we will show that the specific properties of gap solitons generated in the nonlinear driven-dissipative SSH model are strongly linked to the pseudospin evaluated in their core and also in their exponential tails.

To emulate this system with cavity polaritons, we design arrays of coupled micro-pillars (3 µm diameter), with alternating short (2.2 µm) and long (2.75 µm) center-to-center distances, see Fig. 1 (a). This corresponds to effective couplings $J = 0.49\,\text{meV}$ and $J' = 0.20\,\text{meV}$. At the center of some lattices, we create an interface defect by inserting a pillar surrounded by two consecutive long center-to-center distances (see Fig. 1 (c)). These arrays are fabricated by etching an epitaxially grown semiconductor heterostructure that consists in a planar cavity embedding a quantum well (see Methods for more details).

The linear spectrum of these structures is probed by low temperature (4 K) photoluminescence experiments (see Methods). Imaging the emission with angular resolution enables observing polaritonic bands in momentum space (see Fig. 1 (b) and (d)). Real space images are shown in the Supplementary Section S2. The two lowest energy bands take their origin from the hybridization of the s mode of each pillar and emulate the single-particle SSH model with a topological gap of 0.45 meV width. The asymmetry of the spectrum with respect to the center of this gap is attributed to couplings between s and p modes [51]. Interestingly, when the excitation pump overlaps with an interface defect in Fig. 1 (d), a topological state is clearly observed within the topological gap and is localized on the interface pillar (See Fig.S2b in Supplementary materials Section 2).

We first evidence a topological soliton that bifurcates from a topological interface state by focusing the pump on a micropillar defining an interface defect. We tune the laser energy to 180 µeV (approximatively $3\gamma$) above the linear topological edge state and measure the transmitted signal when scanning the excitation power up and down. As shown in Fig. 1 (e),

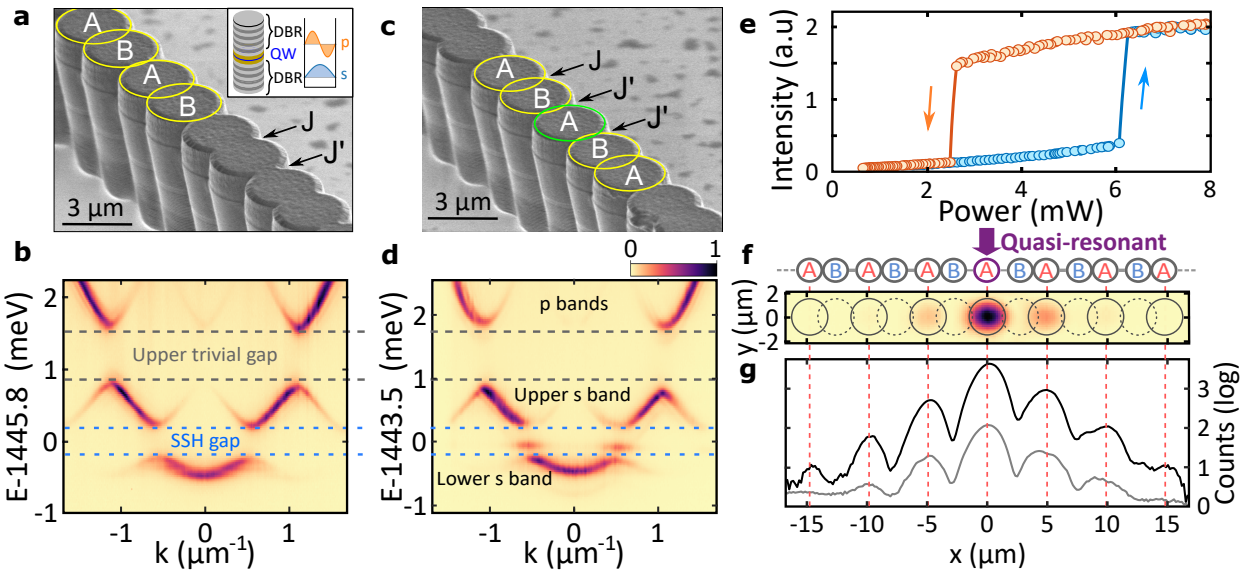


FIG. 1. **Implementation of the SSH lattice. a-c,** Scanning electron microscope images of SSH polariton lattices. We highlight some of the micro-pillars with yellow circles and an interface defect in (c) with a green circle. Inset of (a): Schematic representation of a micro-pillar, composed of a Fabry-Perot cavity defined by two distributed Bragg reflectors (DBR) and a spacer (orange layer) embedding a single quantum well (QW). Right: Typical shape of the $s$ and $p$ polariton modes. **b-d,** Spectrally resolved photoluminescence intensity measured as a function of momentum $k$ under non-resonant excitation using an elongated spot centered in the bulk of lattice (a) (as in panel (b)) and around the interface defect in lattice (c) (as in panel (d)). **e,** Transmitted intensity measured while ramping the excitation power up (blue circles) or down (red circles) under quasi-resonant excitation of the interface defect. **f,** 2D real space image of the transmitted intensity measured on topological soliton. The excitation pump is localized on the interface state, as sketched on top of the panel. **g,** Intensity profiles (integrated along the transverse direction) measured for (grey line) the topological interface state in the linear regime, and (black line) a topological gap soliton bifurcating from the interface state.

an hysteresis cycle is observed in the transmitted intensity, as expected in presence of Kerr nonlinearities. In the high intensity branch of the cycle, we generate a gap soliton that has the same spatial profile as the linear topological interface state (Fig. 1 (g)). This topological soliton shows the expected profile: a core self-localized at the defect position surrounded by two sublattice-polarized exponentially decaying tails.

## BULK GAP SOLITONS

In the following, we address the nonlinear response in the bulk of the SSH lattice, see Fig.1 (a). We implement a quasi-resonant excitation scheme using an excitation laser that is spectrally detuned with respect to the energy $E_0$ of the center of the topological gap by $\Delta E = \hbar\omega - E_0$ (see Fig. 2 (a)). We focus the pump laser (3.5 µm FWHM) ten unit cells away from the lattice edges to avoid finite size effects, and measure the transmitted intensity.

We first consider an excitation scheme where the pump frequency is tuned to the center of the topological gap ($\Delta E = 0$) and is spatially aligned with the center of a dimer. This corresponds, in Eq. (1), to a driving field localized on a single dimer with equal amplitude and phase on both A and B sites. As we ramp up the driving power, we observe the formation of gap solitons that are symmetric with respect to the pump and localized on a discrete number of dimers (see Fig. 2 (b)). When the incident power reaches a first threshold denoted $P_1$, we observe the formation of a bulk soliton with a core extending over one-dimer. Above threshold $P_2$, the soliton core extends to three dimers. Looking at the total transmitted intensity when scanning the power up and down, we evidence bistability and hysteretic behavior at each nonlinear threshold (see Supplementary Section S3). Each threshold occurs when the polariton field locally enters the nonlinear regime, i.e. when the nonlinear blueshift induced by the polariton interaction energy within a dimer overcomes the spectral detuning between the pump and the top of the lower band. These solitons are composed of a self-localized core region (grey-shaded areas in Fig. 2) and of exponentially decaying tails on both sides (white areas). Due to the lattice inversion symmetry, the soliton pseudospin computed over the entire profile vanishes [52]: $\tilde{S}_{\text{tot}} = -0.10 \pm 0.06$ after $P_1$ and $\tilde{S}_{\text{tot}} = 0.09 \pm 0.04$ after $P_2$. Note that variations of the threshold powers are observed when pumping different dimers. They are due to disorder-induced fluctuations of the on-site energy. These fluctuations, on the order of 15 µeV, are smaller than the polariton linewidth ($\gamma \approx 70$ µeV) and do not influence the physics discussed here.

It is insightful to probe how the pseudospin locally varies over the profile. Inside the soliton core, each dimer shows similar amplitude on both sublattices, leading to a locally vanishing pseudospin [52] $\tilde{S}_{\text{core}} = -0.03 \pm 0.09$ after $P_1$ and $\tilde{S}_{\text{core}} = 0.01 \pm 0.06$ after $P_2$, see Fig. 2 (c-d). In contrast, the evanescent tails are strongly localized on a single sublattice: the $A$ sublattice on the left, and the $B$ on the right. Consequently, the pseudo-spins $\tilde{S}_L$ and

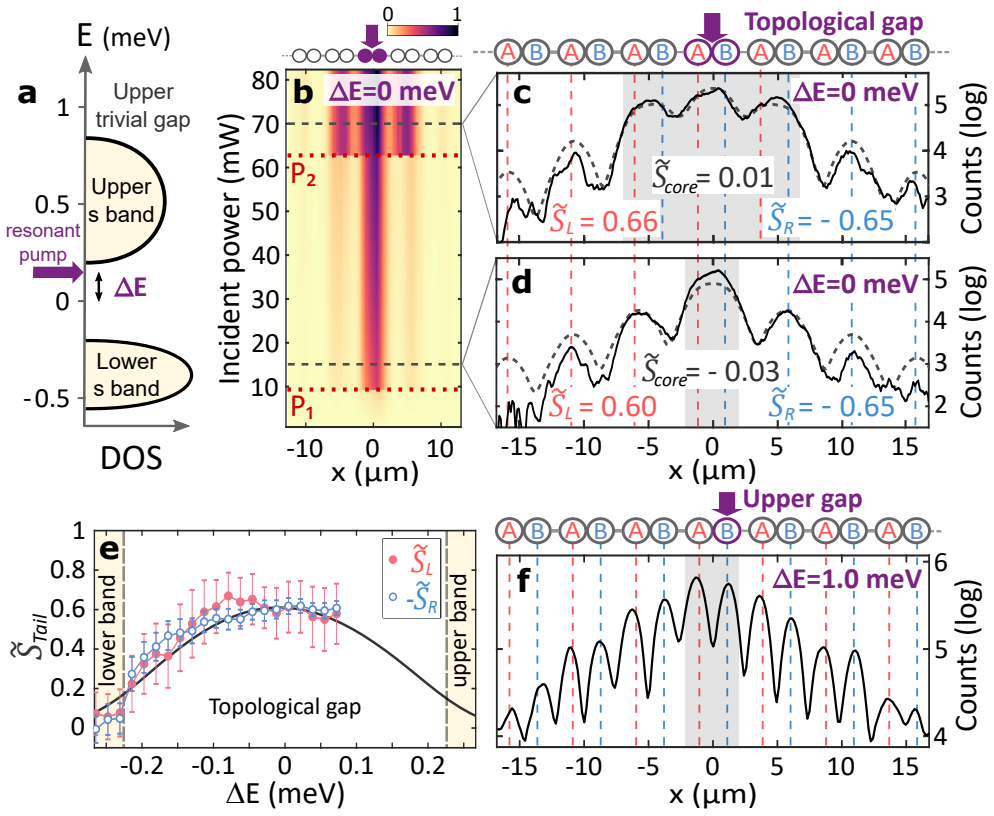


FIG. 2. **Generation of topological gap solitons. a,** Spectral density of states (DOS) of the SSH lattice. The drive (purple arrow) is detuned from the center of the topological gap by $\Delta E$. **b,** Spatially resolved intensity profiles (integrated along the direction perpendicular to the lattice and normalized to their maximum value), measured as we ramp up the driving power. Dotted horizontal red lines mark the $P_1$ and $P_2$ thresholds. **c-d,** Experimental (solid line) and simulated (dashed line) spatial profiles of the soliton above (**c**) $P_2$ and (**d**) $P_1$ thresholds (corresponding excitation powers are indicated with dotted black lines in (b)). **e,** Pseudo-spins $\tilde{S}_L$ (red full circles) and $-\tilde{S}_R$ (blue open circles) measured as a function of $\Delta E$. The amount of optical power available in the experiment enables exploring positive $\Delta E$ values up to 0.1 meV. The grey solid line shows the values of $\tilde{S}_L$ obtained using a tight-binding calculation, where the intensity on each site is convoluted with a Gaussian profile of FWHM 2.7 μm (around the FHWM of the pillar $s$-mode). **f,**. Soliton profile measured when the laser energy is tuned to the upper trivial gap ($\Delta E = 1.0$ meV). In all panels (b,c,d,f), location of the drive is indicated with a purple arrow in the sketch above. In panels (c,d,f), red (blue) dashed lines indicate A (B) sites with peaked intensity, while gray areas represent the extent of the soliton cores.

$\tilde{S}_R$ integrated over the left and right soliton tails do not vanish and present opposite signs: $\tilde{S}_L > 0$ and $\tilde{S}_R < 0$, see Fig. 2 (c-d).

The spin properties of the bulk soliton tails can be further explored when varying the laser energy. In Fig. 2 (e), we report the measured spin polarization $\tilde{S}_L$ and $\tilde{S}_R$ of the left and right evanescent tails when varying $\Delta E$ within the topological gap. When the laser energy departs from the center of the topological gap, the tails remain spin-polarized as long as the laser energy stays within the gap (see Supplemental Section S4 for measured profiles). It vanishes when the excitation reaches the edges of the topological gap. The spin polarization of the tails observed in solitons generated in the topological gap is thus directly linked to the chiral symmetry of the SSH model. To highlight this specific property, we tune the laser energy to the upper gap separating the $s$ and $p$ bands [53]. The soliton profile obtained when exciting this trivial gap is presented in Fig. 2(f). Both evanescent tails present high intensities on all pillars, and thus no spin polarization.

To accurately reproduce the experimental data, we use an effective 1D continuous model, which allows taking into account the finite size of the lattice pillars and the mixing of s-p bands. We look for steady-state solutions of the following Gross-Pitaevskii equation:

$$i\hbar\frac{d\psi(x,t)}{dt} = \left[-\frac{\hbar^2}{2m}\nabla^2 - i\frac{\gamma}{2} + V(x) + g|\psi(x,t)|^2\right]\psi(x,t) + iF(x)e^{-i\omega_p t} \tag{3}$$

where $m$ is the polariton mass. The strong and weak links are respectively represented by barriers of small and large amplitudes in the potential $V(x)$ (see Supplementary Section S5). Numerical results shown in Fig. 2.(c-d) (and also Fig.S6) reproduce the measured soliton profiles with their characteristic tails of opposite spin polarization [54]. Note that since the energy splitting between s and p orbitals is an order of magnitude bigger than the effective coupling between pillars, the deviation from perfect chiral symmetry induced by the s-p coupling (which is taken into account in the 1D continuous model) does not significantly alter the sublattice spin properties of bulk gap solitons.

## ROBUSTNESS OF BULK GAP SOLITONS IN THE PRESENCE OF A NON-HERMITIAN DEFECT

It was theoretically predicted for conservative SSH lattices [23], that these spin-polarized tails play a crucial role in the robustness properties of solitons in the topological gap, and in

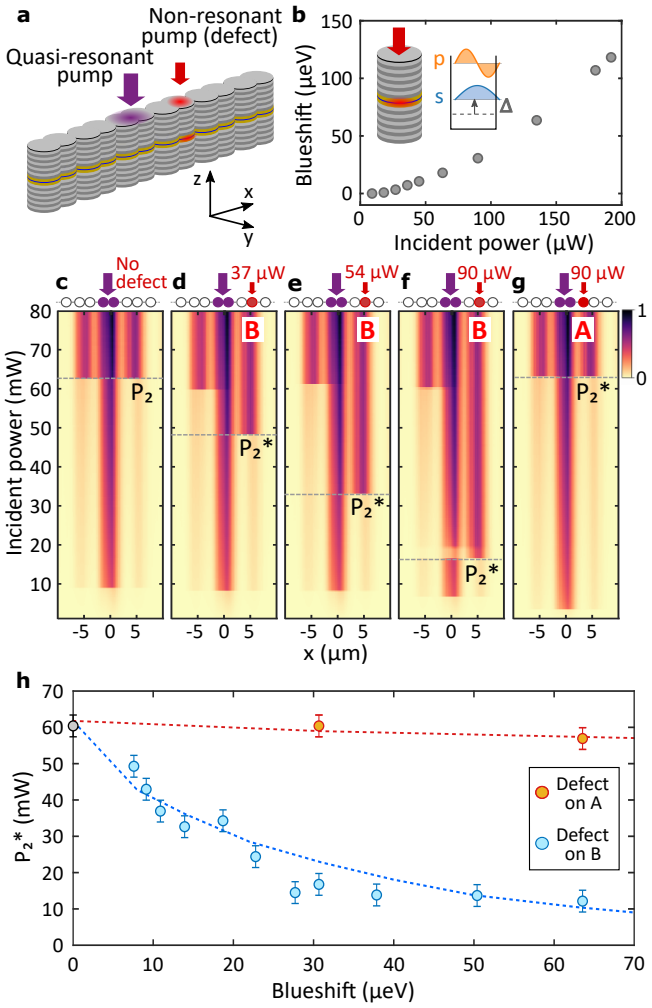


FIG. 3. **Robustness of gap solitons against a defect. a,** Scheme of the two-beam experiment to generate both a soliton (quasi-resonant pump, purple arrow) and an optically induced defect (non-resonant pump, red arrow). **b,** Calibration of the optical defect: blueshift $\Delta$ as a function of the non-resonant pump power measured on an isolated micro-pillar. **c-g,** Spatially resolved intensity profiles (integrated along the direction perpendicular to the lattice and normalized to their maximum value), measured as we ramp up the driving power for (**c**) no defect, (**d-f**) a defect on the $B$ sublattice generated with various non-resonant powers, and (**g**) a defect on the $A$ sublattice generated with same power as in (**f**). For each panel, the driven dimer (defect) is shown on top with purple (red) circles. **h,** Threshold power $P_2^*$ measured as a function of the blueshift (deduced from (**b**)) induced by a defect localized on the $A$ (red symbols) or $B$ (blue symbols) sublattice.The red (blue) line corresponds to numerical simulations.

their interaction with a local defect. Hereafter, we extend this idea to the driven-dissipative framework, and show that the nonlinear threshold for the lateral growth of the soliton core is immune to the presence of a defect on one sublattice but not on the other one.

In order to probe the effect of a perturbation, we consider a defect on a pillar belonging to a dimer neighboring the soliton core. We then monitor how the spatial expansion of the soliton core is affected by this perturbation. The defect is optically generated by non-resonantly pumping a pillar belonging to the A or B sublattice with a second laser (see Fig. 3 a). This creates a local reservoir of excitons whose effect is twofold: 1- it locally blueshifts the pillar on-site energy thus acting as a perturbation on the real part of the potential; and 2- it induces a local gain through stimulated relaxation of excitons toward polariton modes, thus acting as a perturbation of the imaginary part of the potential. This defect is therefore intrinsically non-Hermitian.

To calibrate the real part of this perturbation, we measure the spectral shift of the ground-state emission from a single micro-pillar presenting the same characteristics as the ones forming the chain (see Fig. 3 (b)). For the imaginary part, we evaluate the lasing threshold in the same pillar ($P_{\mathrm{th}} \sim 0.6$ mW), which enables estimating the gain induced by the non-resonant pump creating the defect (see Supplementary Section S7).

The evolution of the spatial profile of solitons as we ramp up the resonant pump power is displayed in Fig. 3 (d)-(g) for different amplitudes and positions of the defect. For comparison, the case with no defect is shown in Panel (c). We first monitor the soliton core expansion in presence of a defect located on a B sublattice site, where the soliton tail intensity presents local maxima (see panels (d)-(f) and Supplementary Section S7 for the calculated profiles). As the defect breaks the system spatial symmetry with respect to the excitation spot, and locally reduces the laser detuning, the soliton core expansion becomes asymmetric. It is first favored toward the defect at power $P_2^*$. At a higher power, close to power $P_2$ measured without defect, the soliton eventually recovers a symmetric profile. We observe in Fig. 3 (h) that $P_2^*$ strongly varies with the defect amplitude. For instance, a defect as small as 20 µeV (less than a tenth of the detuning between the pump laser and the top of the lower s-band) is sufficient to reduce $P_2^*$ by a factor of two with respect to $P_2$. In the simulated curve shown in Fig. 3 (h), this strong sensitivity is well accounted for by including both calibrated values of the real and imaginary parts of the perturbation (see Supplementary Section S7 and Fig.S8).

This high sensitivity to defects located on the $B$ sublattice contrasts with what we measure when the defect is localized on the $A$ sublattice, where the amplitude of the tails vanishes. In that case, the second nonlinear expansion simultaneously occurs toward the right and left dimer, regardless of the defect amplitude (see Fig. 3 (g)-(h)) and for a power close to the one measured in absence of defect. This difference in sensitivity to defects located on $A$ or $B$ sublattice is a direct consequence of the spin polarization of the soliton tails. These results demonstrate that the lattice chiral symmetry provides solitons in the topological gap with high robustness against non-Hermitian defects located on one sublattice. This would also apply to the topological solitons discussed earlier, which bifurcate from a topological edge state. Moreover, as discussed in Ref. [34], linear topological edge states at zero energy are immune to disorder in the SSH lattice coupling constants, as long as the topological gap remains open. These properties still hold for the gap solitons discussed here.

## GENERATING SPIN POLARIZED GAP SOLITONS USING PHASE-ENGINEERED DRIVE

The bulk solitons we have considered so far present a globally vanishing pseudospin, like in conservative systems [52]. Hereafter, we show how we can depart from this family of unpolarized solutions thanks to the driven-dissipative nature of polaritons. To do this, we turn to an excitation scheme where two pillars of a dimer are driven with two beams with same amplitude and tunable phase difference $\Delta\varphi = \varphi_{\mathrm{A}} - \varphi_{\mathrm{B}}$ (see sketch above Fig. 4 (a)). In Eq. (1), this corresponds to a driving field still localized on a single dimer with equal amplitude on both sublattices, but different phases. We select a total excitation power $P > P_2$ in order to obtain a three-dimer soliton when $\Delta\varphi = 0$. Fig. 4 (a) presents the evolution of the intensity distribution along the lattice upon increasing $\Delta\varphi$. A sequence of abrupt switchings is revealed between distinct regimes where the soliton core changes size. Close to $\Delta\varphi = \pi$, the driving field becomes orthogonal to the Bloch modes, strongly reducing light injection into the lattice and explaining why the system switches to the linear regime.

Interestingly, for non-zero values of $\Delta\varphi$, the soliton exhibits a non-zero total sublattice polarization, which reaches a maximum close to $|\tilde{S}_{\mathrm{Tot}}| = 0.5$ in the vicinity of $\Delta\varphi = \pi$ (see Fig. 4 (b)). Remarkably, the soliton core is then localized on a single site of the driven

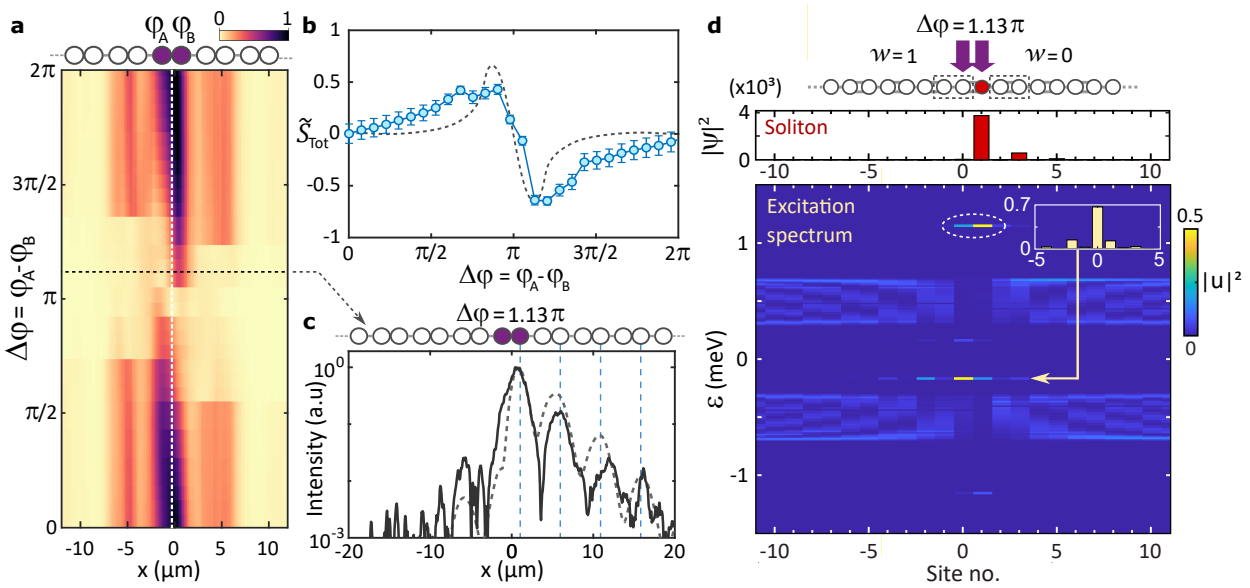


FIG. 4. **Spin-polarized solitons. a,** Spatially resolved intensity profiles (integrated along the direction perpendicular to the lattice and normalized to their maximum value), measured as a function of $\Delta\varphi$ for a total excitation power $P > P_2$ ($P = 80\,\mathrm{mW}$). The driven dimer is depicted on top (purple circles). The white vertical dashed line indicates the center of the driven dimer. **b,** Measured (symbols) and calculated (dashed line) soliton global pseudospin as a function of $\Delta\varphi$ **c,** Intensity profile of the soliton measured (solid line) and simulated (dashed line) for a phase difference $\Delta\varphi = 1.13\,\pi$ (indicated by the horizontal dashed line in Panel **a**). Blue dashed lines mark B pillars with peaked intensity. **d,** Calculated Bogoliubov excitation spectrum (bottom panel) when driving a dimer with $\Delta E = 0$, $\Delta\varphi = 1.13$ and an excitation power corresponding to the maximum spin polarization of the soliton core. The white dashed ellipse highlights the blueshifted mode, and the arrow points towards the mode emerging in the gap (see the mode profile in inset). Above the Bogoliubov spectrum, we show the intensity profile of the bulk soliton (red bars), as well as an illustrative schematics depicting the chain: the red disc shows the site which eigenmode has effectively been decoupled from the bands, while the white discs show the remaining semi-infinite chains together with their respective winding numbers related to the coupling strength at the termination.

dimer, while the other driven site experiences a destructive interference induced by the nonlinearity. We show, in Fig. 4 (c), experimental and theoretical spatial profiles of this soliton for $\Delta\varphi = 1.13\ \pi$. As can be derived analytically (see Supplemental Section 9),

when assuming perfect destructive interference in one of the two sites of the driven dimer, the resulting profile is found to be the same as that of a SSH topological edge state. We emphasize that the novel family of spin-polarized gap solitons we report here does not exist in conservative or undriven systems, as a phase-patterned driving field is required to stabilize them (see Supplementary Section 8).

Highly spin-polarized dissipative solitons have striking consequences on the physics of the underlying excitations. These consequences are related to the nonlinear onsite energy blueshifts locally induced by the solitons. For $\Delta\varphi = 1.13\ \pi$, the soliton core is localized on a single site so that the energy of this particular site is strongly shifted and lies above the upper SSH band. This creates a local potential barrier strongly localized on a single site and effectively splits the lattice in two semi-infinite SSH chains, one of them showing a weak link termination ($\mathcal{W} = 1$). This suggests the optical creation of a non-trivial interface. For a more quantitative analysis of this effect, we compute the Bogoliubov excitation spectrum of the system (see Methods), in presence of a spin-polarized soliton. We consider a situation similar to the experimental one, where the soliton is generated at energy $\Delta E = 0$ using two pumps localized on sites 0 and 1 and $\Delta\varphi = 1.13\ \pi$. The spatial profile of the soliton (obtained for the excitation corresponding to the optimal destructive interference within the driven dimer), is shown in the top part of Fig. 4(d), and the spatial profile of the Bogoliubov modes is shown in the bottom. The Bogoliubov spectrum clearly shows a high energy mode strongly localized at the soliton core position on site 1 (mode highlighted with a white dashed ellipse), which is a signature of the large blueshift experienced by this site. The vanishing amplitude of the Bloch band states at this position hints towards the fact that the lattice has effectively been split into two parts. Remarkably, we observe the emergence of a Bogoliubov mode within the topological gap (see arrow), together with its particle-hole symmetric with respect to the pump energy $E = 0$ [55]. This mode is localized on site 0 (weak link termination with $\mathcal{W} = 1$ next to the soliton core), and presents a strong spin polarization of $\tilde{S} = 0.67$, thus pointing towards the non-trivial character of the optically-created interface. Since the soliton does not create an infinite potential barrier, the emerging topological edge state in the excitation spectrum is not fully spin-polarized as one would expect otherwise if the optical potential barrier were infinite. These simulations appeal for further explorations (beyond the scope of the present paper) to experimentally demonstrate the emergence of an edge state induced by spin-polarized dissipative solitons

in the topological gap of the SSH lattice.

## OUTLOOK

This work provides new perspectives to nonlinear topological photonics. Indeed, we have shown that the driven-dissipative nature of polaritonic systems provides a general way to stabilize novel nonlinear solutions that find no equivalent in conservative systems, to engineer non-Hermitian defects, as well as to reshape the potential landscape probed by Bogoliubov excitations and to modify its topology [56, 57]. The control over the imaginary part of the potential could enable the exploration of PT-symmetric phases in nonlinear driven-dissipative systems [41]. It will also be of the highest interest to extend these ideas in more complex non-Hermitian landscapes with chiral symmetry like 2D polariton lattices [17, 44, 58, 59] or higher-order topological insulators [60–62].

## METHODS

### Sample description

The periodic structure used in this work is etched out of a planar semiconductor microcavity with nominal quality factor of $Q \approx 75,000$ grown by molecular beam epitaxy. The microcavity is composed of a $\lambda$ GaAs layer embedded between two $Ga_{0.9}Al_{0.1}As/Ga_{0.05}Al_{0.95}As$ distributed Bragg reflectors with 28 (top) and 32 (bottom) pairs. A single 15 nm $In_{0.05}Ga_{0.95}As$ quantum well is inserted at the center of the cavity, resulting in strong exciton-photon coupling, with an associated 3.2 meV Rabi splitting (measured by probing the polariton dispersion via angularly resolved photoluminescence as explained in the Supplementary Section 1). After the epitaxy, the sample is processed with electron beam lithography and dry etching into arrays of coupled pillars arranged in a SSH lattice. The exciton-photon detuning, defined as the energy difference between the uncoupled cavity mode at the bottom of the s-band and the exciton resonance, is of the order of $-4.9$ meV for all experiments (see Supplementary Section 1).

### Experimental techniques

The sample is held at $T = 4$ K in a closed-cycle cryostat. Non-resonant photoluminescence measurements are realized with a single-mode continuous-wave laser at 780 nm. The exci-

tation spot is elongated (FWHM $\sim 30\,\mu$m) by focusing the beam with a cylindrical lens at the back-focal plane of the excitation objective. The emission is collected through a lens with NA 0.55 and imaged on the entrance slit of a spectrometer coupled to a charge-coupled device camera with $\sim 30\,\mu$eV spectral resolution. Real- and momentum-space photoluminescence images are realized by imaging the sample surface and the Fourier plane of the objective, respectively. A polarizer is used to select emission polarized along the long axis of the lattice. Experiments with quasi-resonant excitation are realized in transmission geometry, with the excitation (detection) on the epitaxial (substrate) side of the sample and a spot of 3.5 µm FWHM. The optical defect is created by focusing onto a 3 µm FWHM spot a 825 nm cw laser on the epitaxial side. For the resonant two-spot experiment (each with 3.5 µm FWHM), the phase difference is controlled with a delay line with one of the mirrors mounted on a piezoelectric actuator. Error bars in Fig. 3 (h) correspond to the standard deviation on the measurement of $P_2$ obtained by performing a repeatibility study on the resonant pump alignment. Error bars in Fig. 4 (b) are calculated by evaluating the impact of modifications in the area chosen for intensity integration on the pseudo spin calculation.

**Numerical methods**

We use the 3-rd order Adams-Bashforth method for numerical integration of the nonlinear Gross-Pitaevskii Eq. (3) with a time step of $10^{-3}$ ps. CPU-based parallel computing is used to evaluate the kinetic energy term via Fast Fourier Transform. The numerical grid of $2^9 = 512$ points allows to describe a lattice of 21 dimers with a step of 0.25 µm. Increasing the resolution further or considering a longer chain does not change the results. The ramp-up and ramp-down times are 20 ns, which is a compromise between the required adiabaticity and simulation time. We have checked that increasing the ramp-up time further does not change the results. The parameters were as follows: $m = 3 \times 10^{-5} m_0$ ($m_0$ is the free electron mass), $\gamma = 70\,\mu$eV , $g = 5\,\mu\text{eV} \cdot \mu\text{m}^2$ pumping spot FWHM $\approx 2.8\,\mu$m, and the pumping frequency detuning with respect to the band edge is $\approx 0.2\,$meV. Other relevant parameters, such as the potential profile, are provided and discussed in the Supplementary materials. Bogoliubov spectra were calculated by linearizing the discretized Gross-Pitaevskii equation around the steady state solution $\boldsymbol{\psi}^s$ using the ansatz $\boldsymbol{\psi}_n = (\boldsymbol{\psi}^s_n + \delta\boldsymbol{\psi}_n)\exp(i\omega t)$ with $\delta\boldsymbol{\psi}_n = \boldsymbol{u}_n \exp(-i\epsilon t/\hbar) + \boldsymbol{v}^*_n \exp(i\epsilon^* t/\hbar)$, where $\epsilon$ is the complex-valued energy [63] and $\boldsymbol{u}$ and $\boldsymbol{v}$ are two components vectors describing the amplitude of the wavefunction of the A and B sites in the $n^{th}$ unit cell. The spectrum is symmetric with respect to the pump energy

$E = 0\,\mathrm{meV}$, as imposed by particle-hole symmetry. In the graph Fig. 4(d), we display the energy versus position distribution of the component $|\boldsymbol{u}_n|^2$ that is associated to the creation operator. The squared amplitudes corresponding to the A and B sites of the $n^{th}$ unit cell are associated to site numbers $2n$ and $2n+1$, respectively.

**Acknowledgements**

We thank one of the anonymous reviewers for their insightful comments, that led to major improvements of the article. This work was supported by the Paris Ile-de-France Région in the framework of DIM SIRTEQ, the Marie Sklodowska-Curie individual fellowship ToPol, the H2020-FETFLAG project PhoQus (820392), the QUANTERA project Interpol (ANR-QUAN-0003-05), the French National Research Agency project Quantum Fluids of Light (ANR-16-CE30-0021), European Research Council via projects EmergenTopo (865151) and ARQADIA (949730), the French RENATECH network, the French government through the Programme Investissement dAvenir (I-SITE ULNE / ANR-16-IDEX-0004 ULNE) and IDEX-ISITE initiative 16-IDEX-0001 (CAP 20-25), managed by the Agence Nationale de la Recherche, the Labex CEMPI (ANR-11-LABX-0007).

**Author contributions**

N.P. and P.S.-J. performed the experiments and analyzed the data. N.P. performed initial theoretical modelling of the experiments using the tight-binding approach, which led to the discovery of spin-polarized topological solitons. D.D.S and G.M provided theoretical guidance and performed the theoretical calculations in the 1D continuous model. N.P., P.S.-J., D.D.S., G.M, N.C.Z., Q. F., B.R., O.J. A.A., S.R. and J.B. participated to scientific discussions. N.P., P.S.-J., D.D.S., G.M, A.A., S.R. and J.B. wrote the manuscript. N.C.Z. and B.R. contributed to editing of the manuscript. P.S.-J., S. R., J. B. and A.A. designed the sample. A.L., L.L.G., T.B., A.H. and I.S. fabricated the samples. A.A, S.R. and J.B. supervised the work.

**Competing Interests** The authors declare that they have no competing financial interests.

**Correspondence** Correspondence should be addressed to jacqueline.bloch@c2n.upsaclay.fr

---

* These authors contributed equally: N. Pernet, P. St-Jean

[1] Hasan, M. Z. & Kane, C. L. Colloquium: Topological insulators. *Reviews of Modern Physics*

**82**, 3045–3067 (2010).

[2] Qi, X. L. & Zhang, S. C. Topological insulators and superconductors. *Reviews of Modern Physics* **83**, 1057 (2011).

[3] Cooper, N. R., Dalibard, J. & Spielman, I. B. Topological bands for ultracold atoms. *Reviews of Modern Physics* **91**, 015005 (2019).

[4] Lu, L., Joannopoulos, J. D. & Soljačić, M. Topological photonics. *Nature Photonics* **8**, 821–829 (2014).

[5] Ozawa, T. *et al.* Topological photonics. *Reviews of Modern Physics* **91**, 015006 (2019).

[6] Huber, S. D. Topological mechanics. *Nature Physics* **12**, 621–623 (2016).

[7] Peano, V., Brendel, C., Schmidt, M. & Marquardt, F. Topological phases of sound and light. *Physical Review X* **5**, 031011 (2015).

[8] Klembt, S. *et al.* Exciton-polariton topological insulator. *Nature* **562**, 552–556 (2018).

[9] Gianfrate, A. *et al.* Measurement of the quantum geometric tensor and of the anomalous Hall drift. *Nature* **578**, 381–385 (2020).

[10] Ozawa, T. & Price, H. M. Topological quantum matter in synthetic dimensions. *Nature Reviews Physics* **1**, 349–357 (2019).

[11] Meier, E. J. *et al.* Observation of the topological Anderson insulator in disordered atomic wires. *Science* **362**, 929–933 (2018).

[12] Stützer, S. *et al.* Photonic topological Anderson insulators. *Nature* **560**, 461–465 (2018).

[13] Kraus, Y. E., Lahini, Y., Ringel, Z., Verbin, M. & Zilberberg, O. Topological states and adiabatic pumping in quasicrystals. *Physical Review Letters* **109**, 106402 (2012).

[14] Serra-Garcia, M. *et al.* Observation of a phononic quadrupole topological insulator. *Nature* **555**, 342–345 (2018).

[15] Peterson, C. W., Benalcazar, W. A., Hughes, T. L. & Bahl, G. A quantized microwave quadrupole insulator with topologically protected corner states. *Nature* **555**, 346–350 (2018).

[16] Smirnova, D., Leykam, D., Chong, Y. & Kivshar, Y. Nonlinear topological photonics. *Applied Physics Reviews* **7**, 021306 (2020).

[17] Bleu, O., Solnyshkov, D. D. & Malpuech, G. Interacting quantum fluid in a polariton Chern insulator. *Physical Review B* **93**, 085438 (2016).

[18] Hadad, Y., Soric, J. C., Khanikaev, A. B. & Alù, A. Self-induced topological protection in nonlinear circuit arrays. *Nature Electronics* **1**, 178–182 (2018).

[19] Maczewsky, L. J. *et al.* Nonlinearity-induced photonic topological insulator. *Science* **370**, 701–704 (2020).

[20] Mittal, S., Goldschmidt, E. A. & Hafezi, M. A topological source of quantum light. *Nature* **561**, 502–506 (2018).

[21] Kruk, S. *et al.* Nonlinear light generation in topological nanostructures. *Nature Nanotechnology* **14**, 126–130 (2019).

[22] Lumer, Y., Plotnik, Y., Rechtsman, M. C. & Segev, M. Self-localized states in photonic topological insulators. *Phys. Rev. Lett.* **111**, 243905 (2013).

[23] Solnyshkov, D. D., Bleu, O., Teklu, B. & Malpuech, G. Chirality of Topological Gap Solitons in Bosonic Dimer Chains. *Physical Review Letters* **118**, 023901 (2017).

[24] Bisianov, A., Wimmer, M., Peschel, U. & Egorov, O. A. Stability of topologically protected edge states in nonlinear fiber loops. *Phys. Rev. A* **100**, 063830 (2019).

[25] Mukherjee, S. & Rechtsman, M. C. Observation of Floquet solitons in a topological bandgap. *Science* **368**, 856–859 (2020).

[26] Guo, M. *et al.* Weakly nonlinear topological gap solitons in su–schrieffer–heeger photonic lattices. *Opt. Lett.* **45**, 6466–6469 (2020).

[27] Jürgensen, M., Mukherjee, S. & Rechtsman, M. C. Quantized nonlinear thouless pumping. *Nature* **596**, 63–67 (2021).

[28] Jrgensen, M. & Rechtsman, M. C. The chern number governs soliton motion in nonlinear thouless pumps (2021). arXiv:2110.08696.

[29] Mostaan, N., Grusdt, F. & Goldman, N. Quantized transport of solitons in nonlinear thouless pumps: From wannier drags to topological polarons (2021). arXiv:2110.13075.

[30] De Léséleuc, S. *et al.* Observation of a symmetry-protected topological phase of interacting bosons with Rydberg atoms. *Science* **365**, 775–780 (2019).

[31] Clark, L. W., Schine, N., Baum, C., Jia, N. & Simon, J. Observation of Laughlin states made of light. *Nature* **582**, 41–45 (2020).

[32] Bergholtz, E. J., Budich, J. C. & Kunst, F. K. Exceptional topology of non-hermitian systems. *Rev. Mod. Phys.* **93**, 015005 (2021).

[33] Solnyshkov, D. D., Nalitov, A. V. & Malpuech, G. Kibble-zurek mechanism in topologically nontrivial zigzag chains of polariton micropillars. *Phys. Rev. Lett.* **116**, 046402 (2016).

[34] St-Jean, P. *et al.* Lasing in topological edge states of a one-dimensional lattice. *Nature*

*Photonics* **11**, 651–656 (2017).

[35] Zhao, H. *et al.* Topological hybrid silicon microlasers. *Nature Communications* **9**, 1–6 (2018).

[36] Parto, M. *et al.* Complex Edge-State Phase Transitions in 1D Topological Laser Arrays. *Physical Review Letters* **120** (2018).

[37] Bahari, B. *et al.* Nonreciprocal lasing in topological cavities of arbitrary geometries. *Science* **358**, 636–640 (2017).

[38] Bandres, M. A. *et al.* Topological insulator laser: Experiments. *Science* **359**, eaar4005 (2018).

[39] Weimann, S. *et al.* Topologically protected bound states in photonic paritytime-symmetric crystals. *Nature Materials* **16**, 433–438 (2017).

[40] Xia, S. *et al.* Nonlinear tuning of pt symmetry and non-hermitian topological states. *Science* **372**, 72–76 (2021).

[41] Konotop, V. V., Yang, J. & Zezyulin, D. A. Nonlinear waves in PT -symmetric systems. *Reviews of Modern Physics* **88**, 035002 (2016).

[42] Jeon, D. H., Reisner, M., Mortessagne, F., Kottos, T. & Kuhl, U. Non-Hermitian C T -Symmetric Spectral Protection of Nonlinear Defect Modes. *Phys. Rev. Lett.* **125**, 113901 (2020).

[43] Liu, Y. G. N., Jung, P. S., Parto, M., Christodoulides, D. N. & Khajavikhan, M. Gain-induced topological response via tailored long-range interactions. *Nature Physics* **17**, 704–709 (2021).

[44] Bardyn, C. E., Karzig, T., Refael, G. & Liew, T. C. Chiral Bogoliubov excitations in nonlinear bosonic systems. *Physical Review B* **93**, 020502 (2016).

[45] Su, W. P., Schrieffer, J. R. & Heeger, A. J. Solitons in Polyacetylene. *Physical Review Letters* **42**, 1698–1701 (1979).

[46] Tanese, D. *et al.* Polariton condensation in solitonic gap states in a one-dimensional periodic potential. *Nature Communications* **4**, 1–9 (2013).

[47] Cerda-Méndez, E. A. *et al.* Exciton-polariton gap solitons in two-dimensional lattices. *Physical Review Letters* **111**, 146401 (2013).

[48] Whittaker, C. E. *et al.* Effect of photonic spin-orbit coupling on the topological edge modes of a Su-Schrieffer-Heeger chain. *Physical Review B* **99**, 081402 (2019).

[49] Carusotto, I. & Ciuti, C. Quantum fluids of light. *Reviews of Modern Physics* **85**, 299–366 (2013).

[50] Delplace, P., Ullmo, D. & Montambaux, G. Zak phase and the existence of edge states in

graphene. *Phys. Rev. B* **84**, 195452 (2011).

[51] Mangussi, F. *et al.* Multi-orbital tight binding model for cavity-polariton lattices. *Journal of Physics: Condensed Matter* **32**, 315402 (2020).

[52] Smirnova, D. A., Smirnov, L. A., Leykam, D. & Kivshar, Y. S. Topological Edge States and Gap Solitons in the Nonlinear Dirac Model. *Laser & Photonics Reviews* **13**, 1900223 (2019).

[53] To efficiently couple to upper SSH band, we focus the excitation spot onto a single site of a dimer, thus respecting the anti-bonding symmetry of the band.

[54] See Supplementary Section S9 for an analytical derivation of the soliton profile within a tight-binding approach.

[55] Castin, Y. Bose-einstein condensates in atomic gases: Simple theoretical results. *Coherent atomic matter waves* 1136 (1999).

[56] Diehl, S., Rico, E., Baranov, M. A. & Zoller, P. Topology by dissipation in atomic quantum wires. *Nature Physics* **7**, 971–977 (2011).

[57] Bardyn, C.-E. *et al.* Topology by dissipation. *New Journal of Physics* **15**, 085001 (2013).

[58] Kartashov, Y. V. & Skryabin, D. V. Modulational instability and solitary waves in polariton topological insulators. *Optica* **3**, 1228–1236 (2016).

[59] Gulevich, D. R., Yudin, D., Skryabin, D. V., Iorsh, I. V. & Shelykh, I. A. Exploring nonlinear topological states of matter with exciton-polaritons: Edge solitons in kagome lattice. *Scientific Reports* **7**, 1780 (2017).

[60] Mittal, S. *et al.* Photonic quadrupole topological phases. *Nature Photonics* **13**, 692–696 (2019).

[61] El Hassan, A. *et al.* Corner states of light in photonic waveguides. *Nature Photonics* **13**, 697–700 (2019).

[62] Banerjee, R., Mandal, S. & Liew, T. C. H. Coupling between exciton-polariton corner modes through edge states. *Phys. Rev. Lett.* **124**, 063901 (2020).

[63] Sarchi, D., Carusotto, I., Wouters, M. & Savona, V. Coherent dynamics and parametric instabilities of microcavity polaritons in double-well systems. *Phys. Rev. B* **77**, 125324 (2008).